

Electronic Supplementary Information (ESI)

Indoor-Light-Energy-Harvesting Dye-Sensitized Photo-Rechargeable Battery

Byung-Man Kim,^{†a} Myeong-Hee Lee,^{†b} Dilimon Vijayan Sobhana,^b Jeong-Soo Kim,^a Jung Seung Nam,^a Yoon-Gyo Cho,^b Hyun Kuk Noh,^b Deok-Ho Roh,^a Tae-Hyuk Kwon^{*a,b} and Hyun-Kon Song^{*b}

^a Department of Chemistry, Ulsan National Institute of Science and Technology, Ulsan, 44919, Korea

^b School of Energy and Chemical Engineering, Ulsan National Institute of Science and Technology, Ulsan, 44919, Korea

[†] These authors distributed equally.

Corresponding Author

* E-mail: kwon90@unist.ac.kr (T.-H. K); philiphobi@hotmail.com (H.-K. S)

Methods

Materials: All materials were used as received with no purification unless otherwise stated. $\text{Co}^{2+/3+}(\text{bpy})_3(\text{PF}_6)_{2/3}$, and $\text{Cu}^{+/2+}(\text{dmp})_2\text{TFSI}_{1/2}$ were synthesized as described in the literature.¹⁻³ LiMn_2O_4 (LMO; Al-doped; 10 μm in size, Nikki) was surface-graphitized using a high-energy vibratory ball miller (SPEX 8000D) as described in the literature.⁴

Photo-Electrode Fabrication: Fluorine-doped tin oxide (FTO, Nippon Sheet Glass Co., Ltd.) glass was ultrasonically cleaned in the order of acetone, ethanol and DI water for 10 min, respectively. Cleaned FTO glass was treated with 20 min UV- O_3 exposure (UVC-20, Jaesung Engineering Co.) to make surface of FTO hydrophilic and then dipped in 40 mM TiCl_4 (99.9% trace metals basis, Aldrich) aqueous solution at 70 $^\circ\text{C}$ for 30 min to form compact TiO_2 layer. An active TiO_2 layer was prepared by sequentially screen-printing 30 nm diameter TiO_2 particle paste (30NR-D, Greatcell Solar Materials Pty. Ltd.) and reflective TiO_2 particle paste (> 100 nm, Ti-Nanoxide R/SP, Solaronix SA), followed by gradual heating at 150 $^\circ\text{C}$ for 10 min, at 325 $^\circ\text{C}$ for 5 min, at 327 $^\circ\text{C}$ for 5 min, at 450 $^\circ\text{C}$ for 15 min and at 500 $^\circ\text{C}$ for 30 min. The thickness of TiO_2 film (ca. 3.5- μm /4.0- μm) was measured by surface profiler (P6, KLA-Tencor Corporation). The resulting TiO_2 double layer was dipped once more in 40 mM TiCl_4 aqueous solution at 70 $^\circ\text{C}$ for 15 min and heated at 500 $^\circ\text{C}$ for 30 min. After naturally cooled to 80 $^\circ\text{C}$, the TiO_2 electrode was immersed in the dye solution containing 0.2 mM Y123 (Dyename AB) and 1 mM chenodeoxycholic acid ($\geq 97\%$, Aldrich) in $\text{CH}_3\text{CN}/t\text{-BuOH}$ (5:5) at room temperature for 6 h. For co-sensitization, the TiO_2 electrode was pre-immersed in the blue dye solution containing 0.025 mM DN-F10 (Dyename AB) and 10 mM chenodeoxycholic acid in $\text{CH}_3\text{CN}/t\text{-BuOH}$ (5:5) at 40 $^\circ\text{C}$ for 2 h.

Storage-Electrode Fabrication: Storage-electrode was composed of $\text{LMO}@Gn$ as an active material, Super P (Timcal) carbon black as a conduction enhancer and polyvinylidene fluoride (PVdF, SOLVAY Solef 5130) as a binder (weight ratio of 8:1:1) on the 100 nm thick Au-coated FTO. Firstly, PVdF powder was dissolved in *N*-methyl pyrrolidinone (NMP). Grinded mixture of $\text{LMO}@Gn$ and Super P was finely dispersed into the PVdF/NMP solution with stirring. The Au-coated FTO glass was pre-drilled with 1 mm diameter for electrolyte injection and masked using kapton tape (25.4- μm) with the area of 0.6 \times 0.6 cm^2 . The $\text{LMO}@Gn$ slurry was dropped onto the masked substrate, followed by drying at 110 $^\circ\text{C}$ for 1 h and naturally cooling to 25 $^\circ\text{C}$. The loading density of LiMn_2O ranged 1 ~ 1.8 mg/cm^2 .

Cell Assembly: To form a discharge electrode, photo-electrode side of the Li⁺-conductive separator (LICGC™, Ohara Corp.) was Pt-sputtered in a stripe pattern with 50 nm thickness (**Fig. S2**) as a charge collector using FEI-sputter (K575X, EMITECH), followed by electrodeposition of poly(3,4-ethylenedioxythiophene) (PEDOT) on that as a catalytic layer. The electrodeposition was carried out applying a constant current (+0.5 mA) for 30 s in an CH₃CN solution of EDOT containing 0.01 M EDOT (97%, Aldrich) and 0.1 M LiTFSI (Lithium bis(trifluoromethylsulfonyl)imide, 98+%, Fisher Scientific Korea Ltd.). Pt-sputtered Li⁺-conductive separator was attached on a storage-electrode using two sheets of 60 μm Surlyn® resin (Meltonix 1170-60, Solaronix SA) at 110 °C. Then, photo-electrode was attached on that using two sheets of 60 μm Surlyn® resin at 110 °C. Both internal spaces for photo-electrode side and storage-electrode side were filled with three kinds of catholytes and 0.8 M LiClO₄ (99.99% trace metals basis, Aldrich) in CH₃CN, respectively. The I⁻/I₃⁻ catholyte was composed of 0.2 M I₂ (≥ 99.8%, Aldrich), 0.1 M LiI (99.9% trace metals basis, Aldrich), 0.05 M guanidine thiocyanate (≥ 97%, Aldrich), 0.6 M 1,2-dimethyl-3-propylimidazolium iodide (DMPII, Solaronix SA), and 0.5 M 4-tert-butylpyridine (96%, Aldrich) in CH₃CN. The Co^{2+/3+}(bpy)₃ and Cu⁺²⁺(dmp)₂ catholytes were composed of 0.25 M Co²⁺(bpy)₃(PF₆)₂, 0.05 M Co³⁺(bpy)₃(PF₆)₃, 0.1 M LiTFSI, and 0.5 M 4-tert-butylpyridine in CH₃CN and 0.2 M Cu⁺(dmp)₂TFSI, 0.04 M Cu²⁺(dmp)₂TFSI/Cl, 0.1 M LiTFSI, and 0.5 M 4-tert-butylpyridine in CH₃CN, respectively.

Characterization: The absorbance spectra were recorded by the R928 photomultiplier tube of a UV-vis-NIR spectrophotometer (Cary 5000, Agilent Technologies, Inc.). The graphitic layer on the surface of LiMn₂O₄ was observed by high resolution-transmission electron microscopy (HR-TEM, JEM-2100F, JEOL Ltd.). All electrochemical analyses were performed on potentiostats/galvanostats (VMP3, Bio-Logic Science Instruments and 1287A/1260A, Solartron Analytical, AMETEK, Inc.).

Photo-Charging / Galvanostatic Discharging: Photo-charging current was measured using chronoamperometry technique applying 0 V of dc bias under the illumination. Following discharging was carried out using chronopotentiometry technique with various constant currents. Standard AM 1.5G (100 mW cm⁻²) was simulated by photovoltaic efficiency measurement system (IQE-200, Newport Corp.). As indoor light sources, we employed two types of light sources, white light emitting diode (Philips Lighting Korea Ltd.) and compact fluorescent lamp (DSE Co., Ltd.), because both are popularly used energy-saving light sources. We used Si photo-diode (BS-500BK,

Bunkoukeiki Co., Ltd.) and photometer (SPIC-200, HangZhou Everfine Photo-e-info Co., Ltd.) to measure standard AM 1.5G and indoor light intensity, respectively. The photo-active area was controlled by black mask. We adopted $0.4 \times 0.4 \text{ cm}^2$ for standard AM 1.5G and $1.0 \times 0.7 \text{ cm}^2$ for indoor lighting test.

Cyclic Voltammetry: Cyclic voltammetry was carried out at 50 mV s^{-1} of scan rate in a 3-electrode system containing Ag/AgNO₃ as the reference electrode and Pt wire as both working and counter electrodes in a supporting electrolyte (0.1 M LiClO₄ in CH₃CN). Standard reduction potentials were internally referenced versus that of ferrocene/ferrocenium (+0.63 V vs. NHE).

Controlled Intensity Modulated Photo-spectroscopy: To study the photo-current and photo-voltage efficiency frequency response of DSPBs in a photo-charging mode, controlled intensity modulated photo-spectroscopy (CIMPS) technique was carried out on a photoelectrochemical workstation (ZENNIUM XPOT, ZAHNER-elektrik GmbH & Co. KG) equipped with a frequency response analyzer and an automatically intensity-controlled light-emitting diode (503 nm). A small-amplitude sinusoidal pulse (~10% of dc potential) was applied to light source bias with frequency sweep from 10^5 to 10^{-1} Hz.

Linear Sweep Voltammetry and Impedance Spectroscopic Analyses: Linear sweep voltammetry was carried out at 50 mV s^{-1} of scan rate with the symmetric cells consisting of two PEDOT-coated FTO substrates and the electrolyte corresponding to the catholyte in DSPB. Electrochemical impedance spectroscopy was carried out with the same symmetric cells, applying a 10 mV sinusoidal pulse to a dc bias equivalent to the open circuit voltage (0 V) with the frequency sweep from 10^6 to 10^{-1} Hz. All obtained Nyquist plots were fitted with suitable equivalent circuits using ZView software (Scribner Associates, Inc.).

Time Correlated Single Photon Counting: Transient photoluminescence lifetime was measured on fluorescence lifetime spectrometer (FluoTime 300, PicoQuant GmbH), operated in time-correlated single photon counting (TCSPC) mode. The whole system was composed of a Ti:sapphire laser (Mira900, Coherent) with a ~150 fs pulse width and a 76 MHz repetition rate, emission monochromator (SP-2150i), and data acquirer (PicoHarp 300) with photon counting detector (microchannel plate photomultiplier tubes, R3809U-59). Collected decay signals and the instrumental response function were fitted together using an appropriate software (FlouFit, PicoQuant) to acquire the time constant.

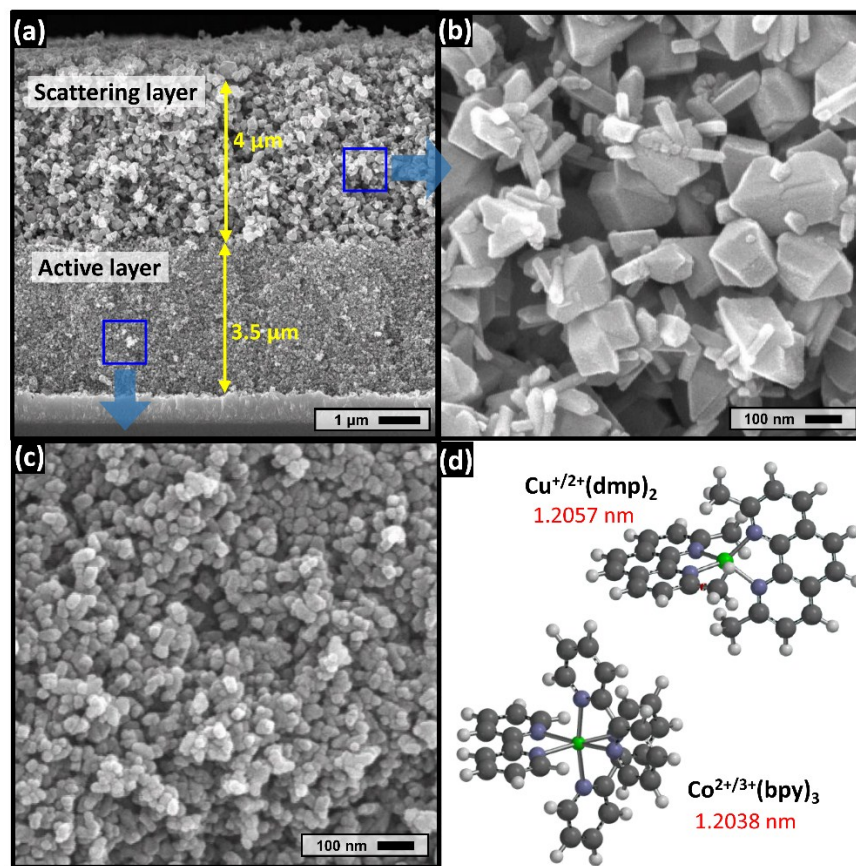


Fig. S1. Materials used in photo-electrodes (PEs). (a to c) Scanning-electron-microscopic images: (a) the cross-sectional view of the photo-electrode; (b) Scattering layer; (c) Active layer. (d) 3D structure of metal complexes used as mediator.

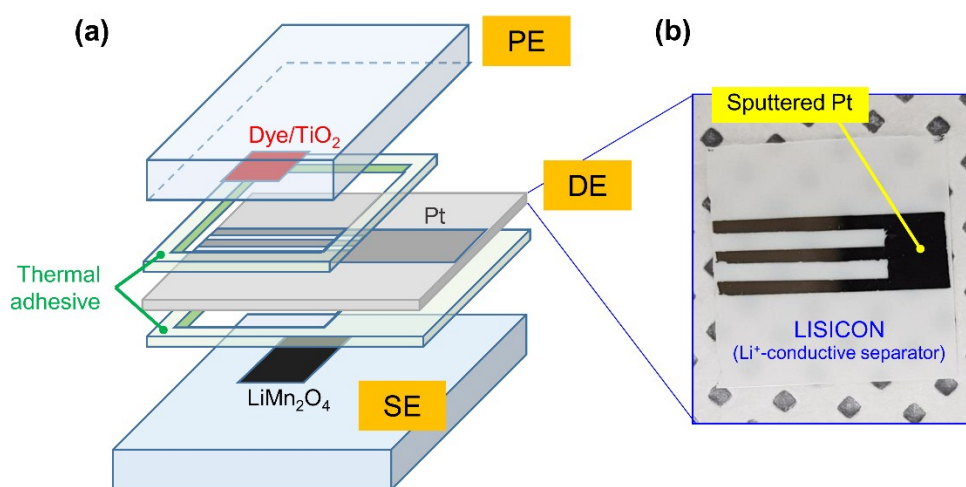


Fig. S2. Design of DSPB. (a) Composition of DSPB. (b) Top-view of discharge electrode (DE) on the Li⁺-conductive separator.

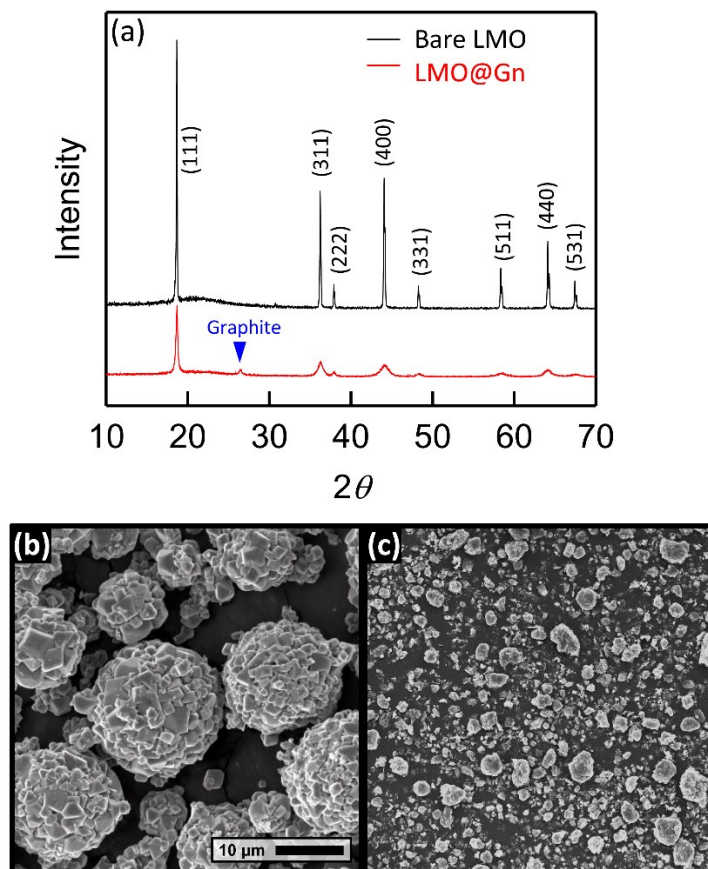


Fig. S3. LMO and LMO@Gn. (a) X-ray diffraction (XRD) patterns. (b and c) Scanning-electron-microscopic images of bare LMO (b) and LMO@Gn (c). The scale bar of (b) is used for (c).

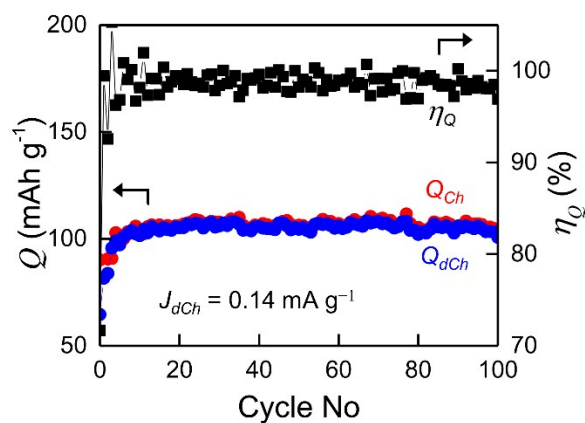


Fig. S4. Cycle durability of LMO@Gn. Charge and discharge are conducted with current density of 0.14 mA g^{-1} .

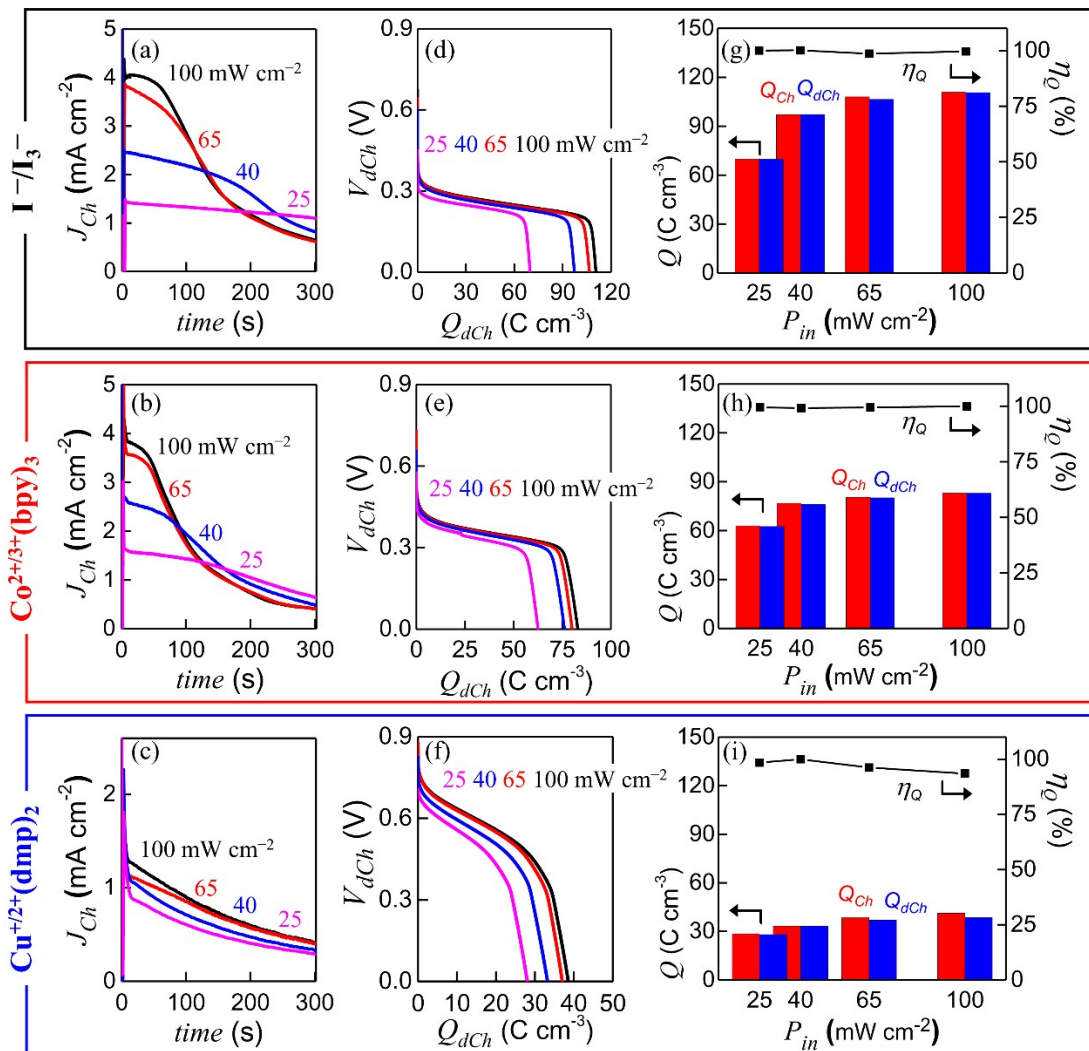


Fig. S5. Light intensity dependency. (a to c) Temporal profiles of photo-charging current. (d to f) Galvanostatic discharge profiles at -0.03 mA cm^{-2} . (g to i) Coulombic efficiency (η_Q).

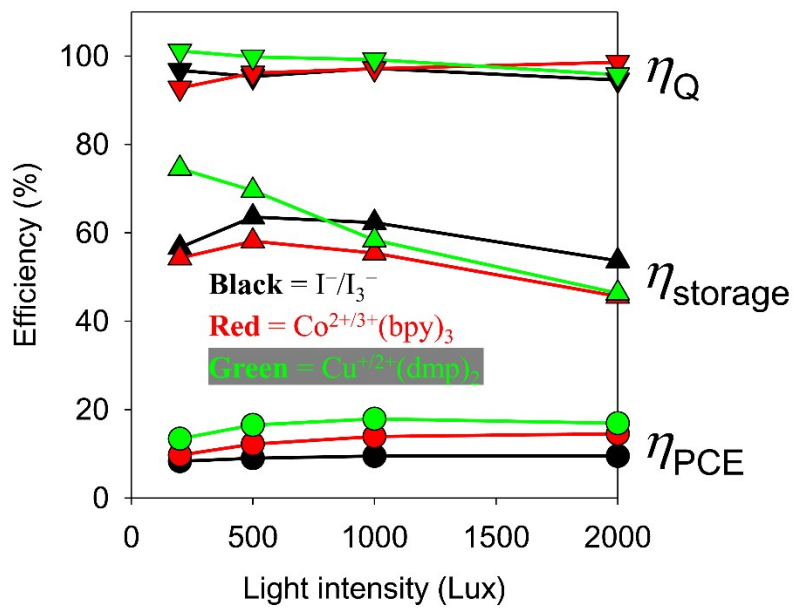


Fig. S6. Efficiencies (η_{PCE} , η_{Storage} and η_Q).

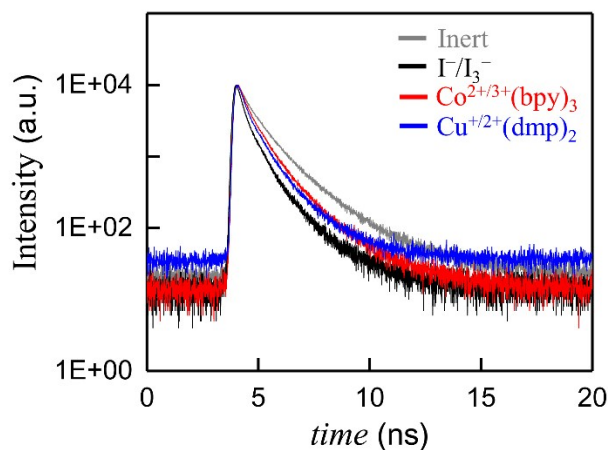


Fig. S7. Regeneration efficiency. PL decay signals detected from Y123 monolayer on Al_2O_3 surrounded by different redox mediators.

The η_{reg} values of Y123 monolayer on Al_2O_3 were estimated by the transient photoluminescence (PL) decay method (**Fig. S7** and **Table S1**).⁵ The conduction band edge of Al_2O_3 is much higher than LUMO level of Y123 so that electron injection from the photo-excited dyes to Al_2O_3 is not allowed. Therefore, the PL signal decay of Y123 on Al_2O_3 between the presence and the absence of a mediator is a measure of the kinetics of electron transfer of not dye-to-substrate but mediator-to-dye (dye regeneration). The estimated values of τ_{ext} in nanosecond were within the range of the reported time scales of dye regeneration.⁶⁻⁸ The I^-/I_3^- showed the highest η_{reg} (81%), followed by $\text{Co}^{2+/3+}(\text{bpy})_3$ and $\text{Cu}^{+/2+}(\text{dmp})_2$ (74% and 72%, respectively). The use of the high- η_{reg} mediator encouraged higher photo-charging current (J_{Ch}) at one sun condition. At dim lights, however, J_{Ch} was independent of mediators characterized by η_{reg} . The number of photon flux at dim-light conditions (e.g., $\sim 1.3 \times 10^{18} \text{ m}^{-2} \text{ s}^{-1}$ of photon flux at 200 lux) is not enough to oxidize all dye molecules on TiO_2 film ($\sim 9.6 \times 10^{19} \text{ m}^{-2}$ of Y123 dye at 2.2- μm). Therefore, the overall kinetics is not limited by the dye regeneration at the dim light conditions.

Table S1. Fitting parameters for estimating average exciton lifetimes of Y123 monolayer on Al₂O₃ and its regeneration efficiencies in the presence of three different mediators.

	A ₁	τ ₁ (ns)	A ₂	τ ₂ (ns)	A ₃	τ ₃ (ns)	τ _{ext} ^a (ns)	η _{reg} ^b
Γ/I ₃ ⁻	11506.7	0.026	2410.1	0.362	381.6	1.322	0.117	0.81
Co ^{2+/3+} (bpy) ₃	5323.6	0.039	1220.2	0.553	325.4	1.594	0.204	0.74
Cu ⁺²⁺ (dmp) ₂	5691.2	0.03	2205	0.385	628.7	1.286	0.214	0.72

^a τ_{ext} = exciton lifetime = $\sum_{i=1}^3 A_i \tau_i$, estimated by fitting the transient PL spectra with the multi-exponential model

$$I(t) = \int_{-\infty}^t IRF(t') \sum_{i=1}^n A_i e^{-(t-t')/\tau_i} dt'$$

by using FlouFit software:

IRF(*t'*) = experimentally measured instrument response function (lamp function)

A_i = amplitude of the *i*th component at time zero in counts

τ_{*i*} = lifetime of the *i*th component

t = time shift between *IRF*(*t'*) and decay.

n = 3 in our calculation.

^b η_{reg} = regeneration efficiency = $1 - \left(\tau_{ext}^{redox} / \tau_{ext}^{inert} \right)$, τ_{ext}^{redox} and τ_{ext}^{inert} = exciton lifetime of dyes in the presence and absence of a redox mediator in the electrolyte, respectively.

The evaluation of electrochemical kinetic parameters

For the measurements, we prepared symmetric cell that consists of two PEDOT-coated FTO electrodes and the electrolyte as depicted in **Fig. S8a**. The rate constant (k_0) for charge transfer near electrode surface and ionic diffusion coefficient (D) values were evaluated using linear sweep voltammetry (LSV) technique and summarized in **Fig. 3** (see **Fig. S8** caption for procedure). For both factors, symmetric cells containing I^-/I_3^- electrolyte always give the highest values, indicative of the fastest reaction and diffusion of I^-/I_3^- . The impedance spectroscopy analysis strongly supports LSV results in terms of electrode/electrolyte interface impedance and Nernst diffusion impedance. **Fig. S8c** and **S8d** present Nyquist plots obtained from symmetric cells with different mediator and equivalent circuit we adopted for fitting, respectively. It is apparent that all mediators feature two semicircles in impedance spectra. Nyquist plots obtained from the symmetric cells are generally composed of two semicircles, corresponding to charge transfer resistance at the electrode/electrolyte interface ($R_{CT, Ed/EI}$) at high frequency region and Warburg impedance in the electrolyte (W_{bulk}) at low frequency region, respectively. If the electrode surface has a porous structure, additional element should be introduced to circuit to consider Warburg impedance within the electrode pores (W_{pore}).⁹ This element has been known to appear at higher frequency region than that of $R_{CT, Ed/EI}$. For all mediators, diffusion limitation in PEDOT pore is negligible and thus the W_{pore} do not appear. All $R_{CT, Ed/EI}$ and W_{bulk} values are summarized in **Fig. 3**. It is noteworthy that the tendency of both R_{CT} and W_{bulk} is consistent with that of kinetics and mass transfer parameters (k_0 and D) obtained from the LSV.

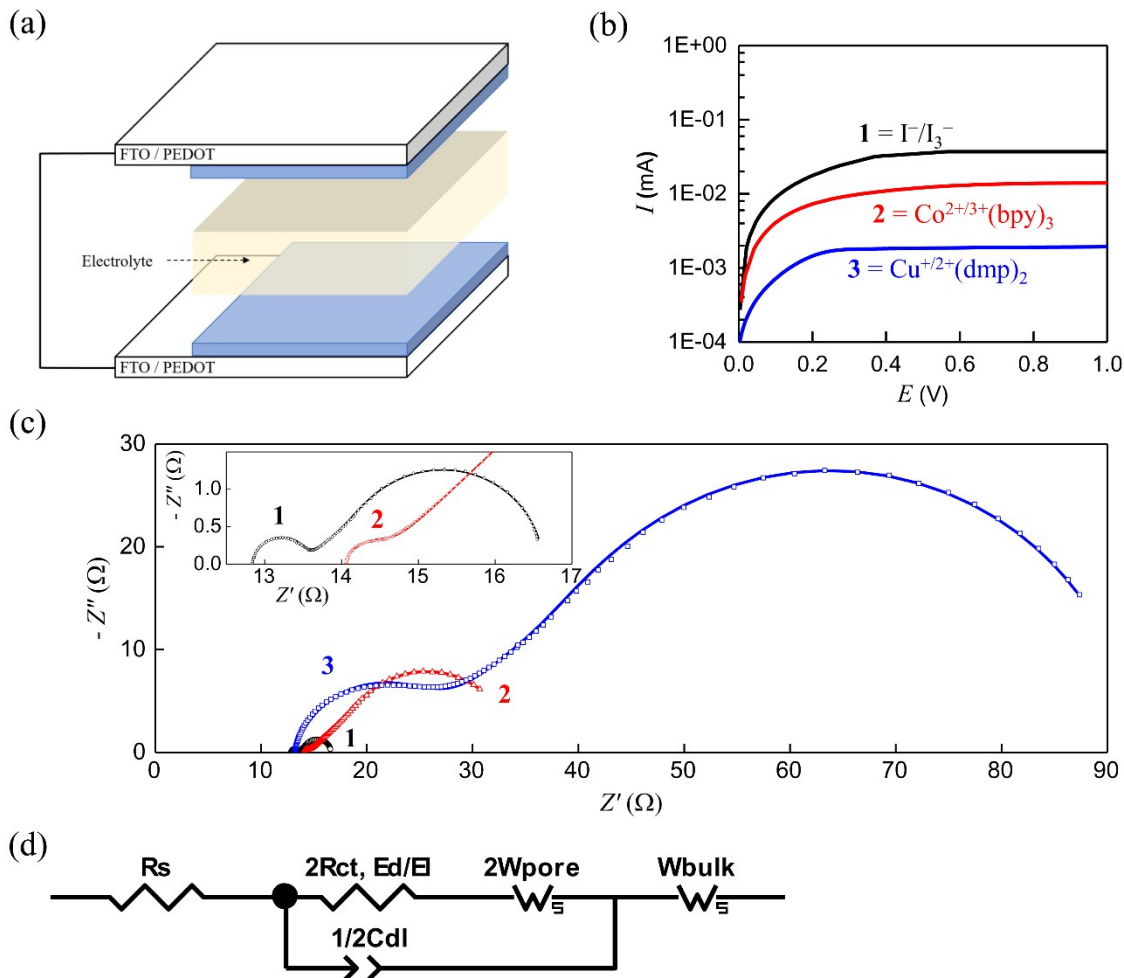


Fig. S8. Reactivity and diffusion ability of redox mediators. (a) Structure of symmetric cell for (b) linear sweep voltammetry and (c) impedance analyses for rate constant (k_0) and ionic diffusion coefficient (D) of redox mediators. k_0 and D were estimated using exchange current (I_0) and limiting current (I_{lim}) as following equation 1 and 2: $I_0 = nFAk_0C_O^{1-\alpha}C_R^\alpha$ (eq. 1) and $I_{lim} = 2nFAC_RD/\delta$ (eq. 2), where n is the number of electrons transferred in the electrochemical reaction, F is the faraday constant, A is the active area, C_O and C_R are bulk concentrations of redox species, α is the transfer coefficient (≈ 0.5), and δ is the distance between electrodes. (d) Equivalent circuit adopted for fitting impedance spectra.

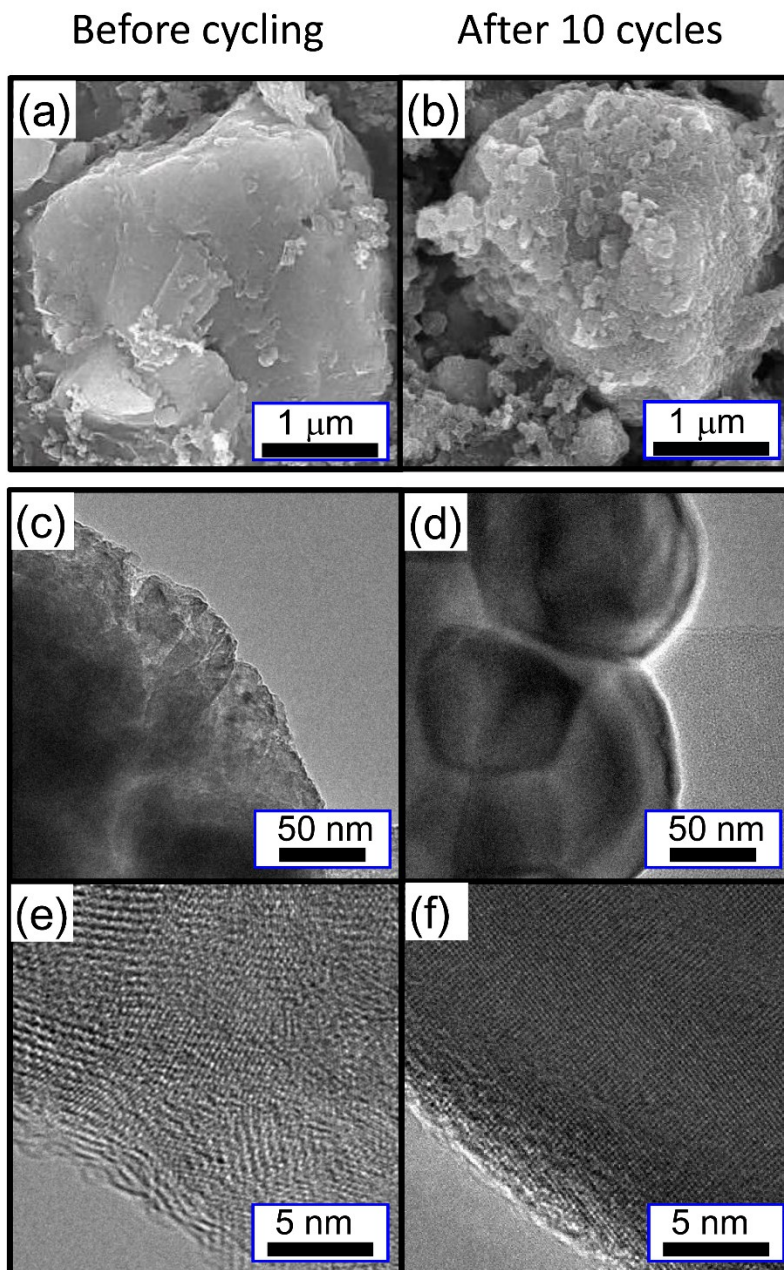


Fig. S9. Electron-microscopic images of LMO@Gn loaded on electrodes before cycling (left column) and after 10 cycles (right column). (a and b) SEM images. (c to f) TEM images.

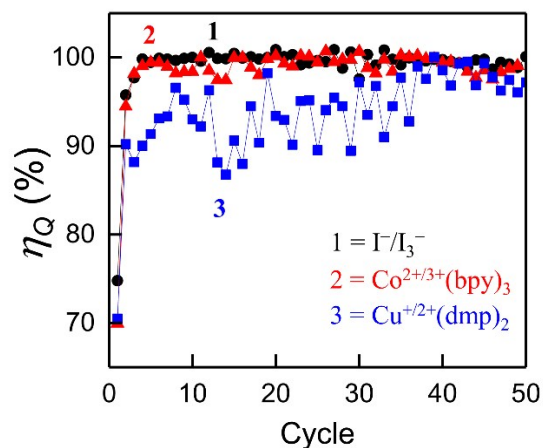


Fig. S10. The charge-to-discharge efficiency (η_Q) at one sun illumination along repeated cycles. The DSPB cells containing the indicated mediators were photo-charged during 5 min and then galvanostatically discharged at 0.03 mA cm^{-2} .

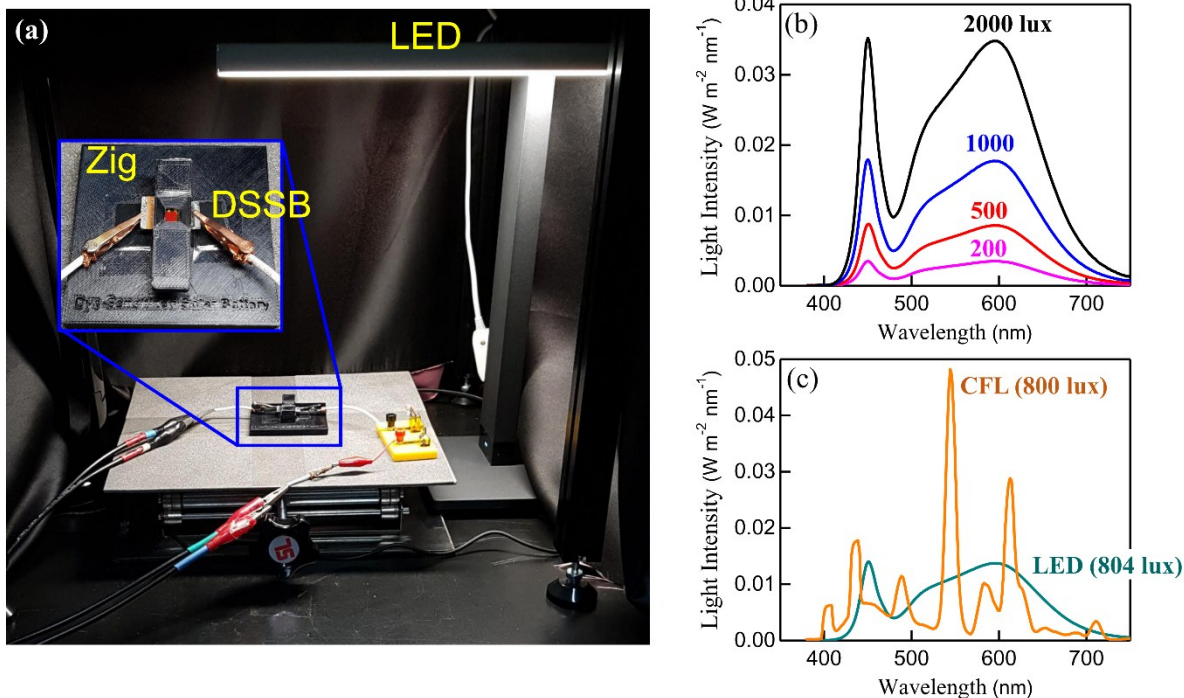


Fig. S11. Indoor lighting system. (a) Home-made indoor lighting system using a white light emitting diode (LED) or a compact fluorescent lamp (CFL). (b) The power spectra of LEDs at various illuminance: 200 lux (0.063 mW cm^{-2}), 500 lux (0.154 mW cm^{-2}), 1000 lux (0.316 mW cm^{-2}) and 2000 lux (0.604 mW cm^{-2}). (c) The power spectrum of the CFL at 800 lux (0.236 mW cm^{-2}). The power spectrum of the LED at the same illuminance was included for comparison.

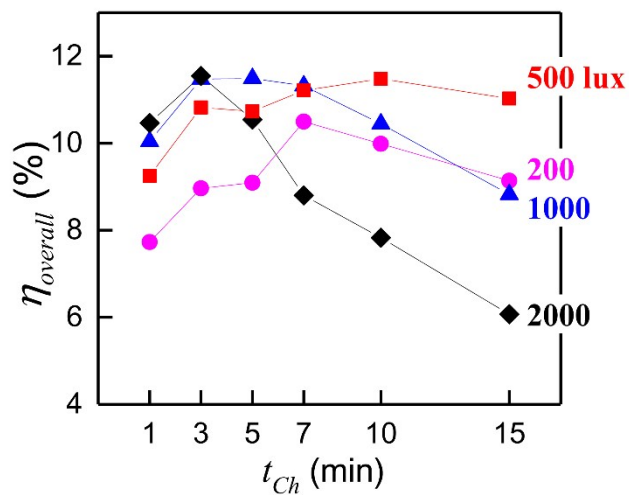


Fig. S12. Photo-charging time dependency under indoor light (LED). Light-to-charge energy efficiencies ($\eta_{overall}$) of DSPB containing $\text{Cu}^{+/2+}(\text{dmp})_2$ mediator as a function of the photo-charging duration under the white LED.

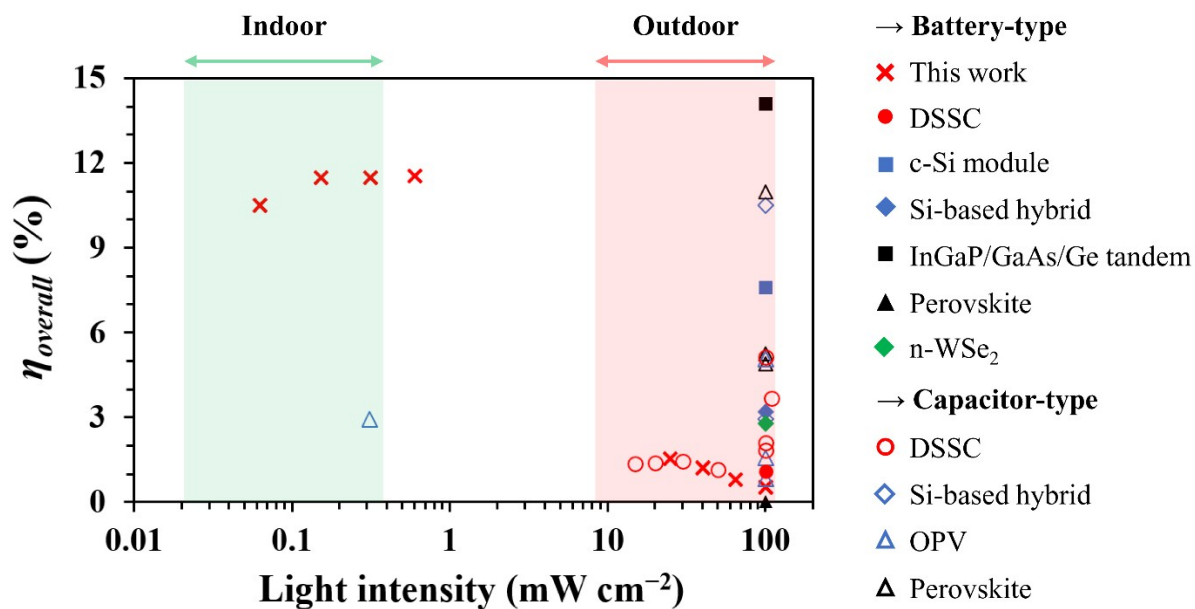


Fig. S13. Overall efficiencies of the state-of-the-art photo-rechargeable systems. The overall efficiencies versus incident light intensity for the state-of-the-art photo-rechargeable systems with different photo-energy harvester, where solid and blank figures represent battery-type¹⁰⁻¹⁷ and capacitor-type¹⁸⁻²⁹ systems, respectively. We show only single-structured systems excluding wire-connected systems. It is apparent that most precedent works do not contribute to indoor part.

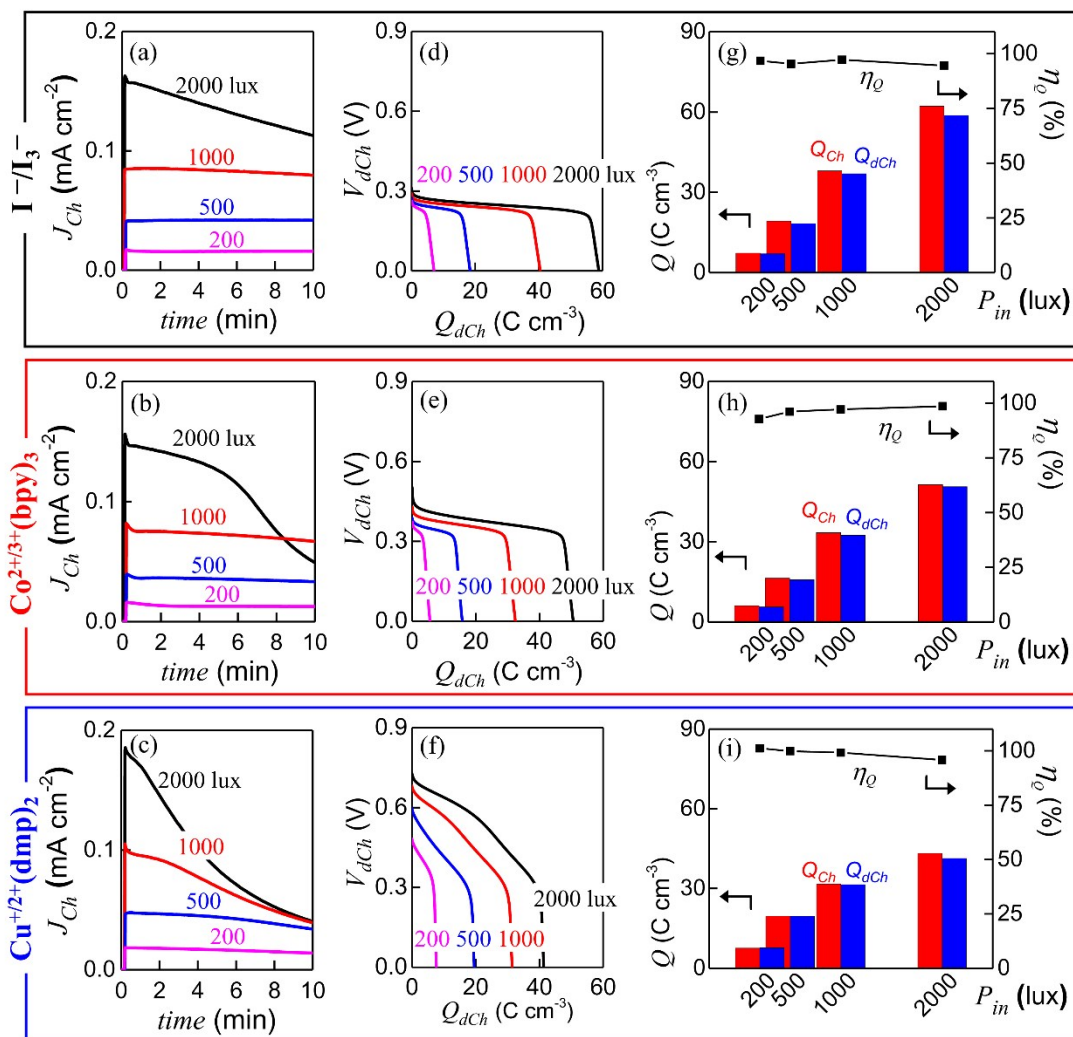


Fig. S14. Light intensity dependency at indoor lighting. (a to c) Temporal profiles of photocurrent. (d to f) Galvanostatic discharge profiles at $-3 \mu A cm^{-2}$. (g to i) Coulombic efficiency (η_Q).

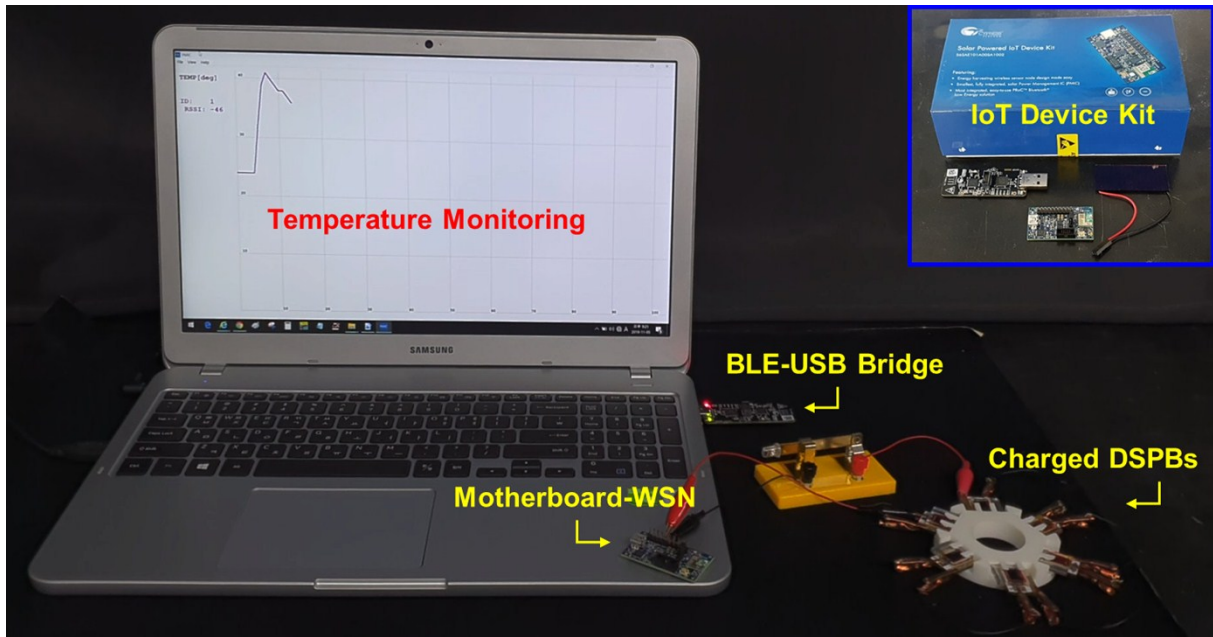


Fig. S15. A DSPB-powered IoT device kit. IoT device kit (S6SAE101A00SA1002, Cypress Semiconductor Corp.) that consisted of motherboard including wireless sensor node (WSN), Bluetooth low energy (BLE)-USB bridge, and silicon solar module was operated by only DSPBs without solar module to monitor temperature. Refer to the **Supporting video clip-2**. In short, six DSPB cells were series-connected in charge mode (PE-SE) and photo-charged at 1000 lux for 10 min. For device operation, they were series-connected in discharge mode (SE-DE) to meet the operating voltage (> 3.5 V). The BLE-USB bridge started to receive signals from the motherboard, observable by blue LED blinking. Heating the sensor in the motherboard by a dryer, the temperature rapidly increased and decreased as soon as a dryer was removed.

References

- 1 S. M. Feldt, E. A. Gibson, E. Gabrielsson, L. Sun, G. Boschloo and A. Hagfeldt, *J. Am. Chem. Soc.*, 2010, **132**, 16714-16724.
- 2 Y. Bai, Q. Yu, N. Cai, Y. Wang, M. Zhang and P. Wang, *Chem. Commun.*, 2011, **47**, 4376-4378.
- 3 M. Freitag, Q. Daniel, M. Pazoki, K. Sveinbjörnsson, J. Zhang, L. Sun, A. Hagfeldt and G. Boschloo, *Energy Environ. Sci.*, 2015, **8**, 2634-2637.
- 4 H. K. Noh, H.-S. Park, H. Y. Jeong, S. U. Lee and H.-K. Song, *Angew. Chem. Int. Ed.*, 2014, **53**, 5059-5063.
- 5 M. Y. Jin, B. M. Kim, H. S. Jung, J. H. Park, D. H. Roh, D. G. Nam, T. H. Kwon and D. H. Ryu, *Adv. Funct. Mater.*, 2016, **26**, 6876-6887.
- 6 C. Nasr, S. Hotchandani and P. V. Kamat, *J. Phys. Chem. B*, 1998, **102**, 4944-4951.
- 7 I. Montanari, J. Nelson and J. R. Durrant, *J. Phys. Chem. B*, 2002, **106**, 12203-12210.
- 8 M. Grätzel, *Inorg. Chem.*, 2005, **44**, 6841-6851.
- 9 J. D. Roy-Mayhew, D. J. Bozym, C. Punckt and I. A. Aksay, *ACS Nano*, 2010, **4**, 6203-6211.
- 10 W. Guo, X. Xue, S. Wang, C. Lin and Z. L. Wang, *Nano Lett.*, 2012, **12**, 2520-2523.
- 11 M. A. Mahmoudzadeh, A. R. Usqaocar, J. Giorgio, D. L. Officer, G. G. Wallace and J. D. W. Madden, *J. Mater. Chem. A*, 2016, **4**, 3446-3452.
- 12 S. Ahmad, C. George, D. J. Beesley, J. J. Baumberg and M. De Volder, *Nano Lett.*, 2018, **18**, 1856-1862.
- 13 H.-D. Um, K.-H. Choi, I. Hwang, S.-H. Kim, K. Seo and S.-Y. Lee, *Energy Environ. Sci.*, 2017, **10**, 931-940.
- 14 W. Li, H. C. Fu, L. Li, M. Cabán-Acevedo, H. He Jr and S. Jin, *Angew. Chem. Int. Ed.*, 2016, **55**, 13104-13108.
- 15 S. Liao, X. Zong, B. Seger, T. Pedersen, T. Yao, C. Ding, J. Shi, J. Chen and C. Li, *Nat. Commun.*, 2016, **7**, 11474.
- 16 J. R. McKone, F. J. DiSalvo and H. D. Abruña, *J. Mater. Chem. A*, 2017, **5**, 5362-5372.
- 17 W. Li, H.-C. Fu, Y. Zhao, J.-H. He and S. Jin, *Chem*, 2018, **4**, 2644-2657.
- 18 Z. Yang, J. Deng, H. Sun, J. Ren, S. Pan and H. Peng, *Adv. Mater.*, 2014, **26**, 7038-7042.
- 19 Z. Yang, L. Li, Y. Luo, R. He, L. Qiu, H. Lin and H. Peng, *J. Mater. Chem. A*, 2013, **1**, 954-958.
- 20 A. Scalia, F. Bella, A. Lamberti, S. Bianco, C. Gerbaldi, E. Tresso and C. F. Pirri, *J. Power Sources*, 2017, **359**, 311-321.
- 21 F. Khatun, P. Thakur, A. Kool, S. Roy, N. A. Hoque, P. Biswas, B. Bagchi and S. Das, *Langmuir*, 2019, **35**, 6346-6355.
- 22 A. P. Cohn, W. R. Erwin, K. Share, L. Oakes, A. S. Westover, R. E. Carter, R. Bardhan and C. L. Pint, *Nano Lett.*, 2015, **15**, 2727-2731.
- 23 Z. Zhang, X. Chen, P. Chen, G. Guan, L. Qiu, H. Lin, Z. Yang, W. Bai, Y. Luo and H. Peng, *Adv. Mater.*, 2014, **26**, 466-470.
- 24 J. Kim, S. M. Lee, Y.-H. Hwang, S. Lee, B. Park, J.-H. Jang and K. Lee, *J. Mater. Chem. A*, 2017, **5**, 1906-1912.
- 25 B. P. Lechêne, M. Cowell, A. Pierre, J. W. Evans, P. K. Wright and A. C. Arias, *Nano Energy*, 2016, **26**, 631-640.
- 26 Z. Liu, Y. Zhong, B. Sun, X. Liu, J. Han, T. Shi, Z. Tang and G. Liao, *ACS Appl. Mater. Interfaces*, 2017, **9**, 22361-22368.

- 27 F. Zhang, W. Li, Z. Xu, M. Ye, H. Xu, W. Guo and X. Liu, *Nano Energy*, 2018, **46**, 168-175.
- 28 H. Liu, M. Li, R. B. Kaner, S. Chen and Q. Pei, *ACS Appl. Mater. Interfaces*, 2018, **10**, 15609-15615.
- 29 R. Liu, J. Wang, T. Sun, M. Wang, C. Wu, H. Zou, T. Song, X. Zhang, S. T. Lee, Z. L. Wang and B. Sun, *Nano Lett.*, 2017, **17**, 4240-4247.